Lithosphere

Research Article

Shear-Wave Splitting Analysis Using Optimization Algorithms

Zhengtao He,[1] **Yuyong Yang** (ID),[2] **and Huailai Zhou**[1]

[1]*College of Geophysics, Chengdu University of Technology, Chengdu 610059, China*
[2]*State Key Laboratory of Oil and Gas Reservoir Geology and Exploitation, Chengdu University of Technology,*
 Chengdu 610059, China

Correspondence should be addressed to Yuyong Yang; yangyuyong19@cdut.edu.cn

Shear-wave splitting (SWS) analysis is used to predict fractures in subsurface media. Specifically, two parameters relevant to SWS analysis (the azimuth of the fast shear wave and the time delay between the fast and slow shear waves) are used to quantify the main azimuth and degree of the fracture development, respectively. However, the algorithms of SWS analysis using a grid search have relatively low computational efficiency, as they need to calculate the objective function values of all grid points. To improve the efficiency of SWS analysis, we proposed new algorithms using the gradient descent, Newton, and advance-retreat methods. The new methods use the direction of the fastest gradient descent, the intersection points of the tangent plane of the first-order objective function with the zero plane, and narrowing the range of extremum points to determine the search path. Therefore, this removes the necessity to compare all grid points in the value region. We compared the three methods and the rotation-correlation method, and both synthetic and field data tests indicated that all three methods had higher computational efficiency than the traditional grid search method. Among the proposed methods, the gradient-descent method obtained the most accurate results for both synthetic and field data. Our study shows that SWS analysis combined with the gradient-descent method can accurately and efficiently obtain SWS parameters for fracture prediction.

1. Introduction

In carbonate and unconventional reservoirs (e.g., tight shale and oil reservoirs), fractures not only connect isolated pores and increase the effective porosity of the reservoir but also provide an important space for oil and gas migration [1] and can improve the permeability of the reservoir [2, 3]. When a shear wave passes through strata containing fractures and the polarization direction of the shear wave is oblique to the azimuth of fractures, it splits into fast and slow shear waves; this action is referred to as the birefringence phenomenon [4]. The delay time between fast and slow shear waves is related to fracture density, and the polarization direction of the fast shear wave is parallel to the fracture plane [5–9]. At present, shear-wave splitting (SWS) analysis is a commonly used and effective method for predicting fractures [10–12].

However, when geophones receive the two shear waves, the fast and slow shear waves are coupled [13, 14]. There-fore, the polarization direction of the fast shear wave and the delay time cannot be determined directly [15, 16] and require calculation through SWS analysis. Alford [17] proposed a method to minimize energy in the off-diagonal elements (xy and yx components) of the data matrix by rotating a series of azimuths in the source and receiver axes, obtaining an accurate azimuth and delay time. When strata with different depths contain fractures in different directions, shear waves passing through multiple fractured strata can result in multiple splits, leading to the inaccuracy of the method mentioned above [18]. Winterstein and Meadows [5] proposed the layer-stripping method to solve this problem. Subsequently, Li and Crampin [19] suggested a linear-transform technique as an alternative to the rotation-scanning technique, in which the complex motion of shear wave is transformed into linear motion. To overcome the asymmetry of the seismic data matrix and wave polarization, singular value decomposition (SVD) [20] and eigenvector-eigenvalue decomposition (EED) [21, 22] were developed.

However, the influence of a low signal-to-noise ratio does not allow the polarization directions of the split shear waves to be estimated accurately through the SVD and EED methods, which leads to deterioration in the separation of the split shear waves [23, 24]. During the same period, a series of scanning algorithms with different objective functions emerged: the tangential energy [25–27], covariance matrix [28–30], and rotation-correlation methods [31–34]. All scanning methods perform a grid search to determine the SWS parameters (polarization azimuth of fast shear waves θ and delay time Δt), but the calculation efficiency is generally low owing to the calculation by increment.

In recent years, many geophysical inversions have been proposed based on optimization algorithms, such as the Gauss-Newton method used by Lu et al. to build a model update matrix and objective function [35], the gradient method applied by Moghaddam et al. to construct a faster and smoother model misfit reduction [36], and the advance-retreat method used by Xiao et al. to determine filter length [37]. The application of these combined optimization algorithms can solve partial complex problems.

Using the gradient descent, Newton, and advance-retreat algorithms can also improve the calculation efficiency [38–40]. Therefore, we proposed three SWS analysis methods based on the three optimization principles and designed the objective function to obtain the best results. Then, we evaluated the accuracy and computational efficiency of the three methods for synthetic and field data. The results showed that the three methods can effectively solve the issue of low computational efficiency while the gradient-descent method ensures accuracy by comparing the inversion results of the three methods with the fracture porosity.

2. Methods

2.1. Rotation-Correlation Method. The application of the rotation-correlation method is prominent [41–49] and can remove the effect of splitting [50]. As the P-wave reaches the reflection interface, it generates an upward converted shear wave (Figure 1). When the polarization direction of the shear wave is tilted with the fracture plane, it splits into a group of orthogonal fast and slow S-waves [51]. The upward direction of the fast and slow shear waves is nearly vertical to the ground, and the fast shear wave reaches the surface faster than the slow one. The R and T components of the three-component geophone can receive the mixed signals of fast and slow shear waves on the ground. The direction of the R component is parallel to the source-geophone direction, and the direction of the T component is orthogonal to the source-geophone direction.

When the converted shear wave, $S(t)$, is obliquely polarized to the fracture plane, the following equation is used to calculate the wavefield:

$$\begin{bmatrix} S1(t) \\ S2(t - \Delta t) \end{bmatrix} = \begin{bmatrix} \cos \theta \\ -\sin \theta \end{bmatrix} S(t), \qquad (1)$$

where θ and Δt are two SWS parameters [52], and $S1(t)$ and $S2(t)$ are the time series of the fast and slow shear waves, respectively. The R and T components can be expressed by θ and $S(t)$ through vector transformation:

$$\begin{bmatrix} R(t) \\ T(t) \end{bmatrix} = \begin{bmatrix} \cos \theta & \sin \theta \\ \sin \theta & -\cos \theta \end{bmatrix} \begin{bmatrix} S1(t) \\ S2(t - \Delta t) \end{bmatrix}. \qquad (2)$$

We multiply Equation (2) by the inverse of the θ matrix to obtain

$$\begin{bmatrix} S1(t) \\ S2(t - \Delta t) \end{bmatrix} = \begin{bmatrix} \cos \theta & \sin \theta \\ \sin \theta & -\cos \theta \end{bmatrix}^{-1} \begin{bmatrix} R(t) \\ T(t) \end{bmatrix}. \qquad (3)$$

Thus, $S1(t)$ and $S2(t-\Delta t)$ can be obtained from the field-received R and T components.

Finally, the objective function is constructed based on the correlation of the fast and slow shear waves:

$$\mathrm{COV}(\theta, \Delta t) = \frac{\sum \left(S1(t) - \overline{S1(t)} \right) \left(S2(t) - \overline{S2(t)} \right)}{\sqrt{\sum \left(S1(t) - \overline{S1(t)} \right)^2 \sum \left(S2(t) - \overline{S2(t)} \right)^2}}, \qquad (4)$$

where $\overline{S1(t)}$ and $\overline{S2(t)}$ are the average values of $S1(t)$ and $S2(t)$ within a time window, respectively. Then, the COV values of all grid points were calculated to determine reasonable θ and Δt (COV = 1) as SWS parameters [53].

The rotation-correlation method is a grid search method which is used to search for the maximum cross-correlation coefficient; further, it derives the splitting time from the delay time corresponding to maximum cross-correlation coefficient [54]. This method's calculation efficiency is low because the COV values must be computed from 0° to 180° with an increment of 1° [55–57]. At present, many optimization algorithms can quickly search for the extremum point of the objective function. Therefore, we have taken the COV as the objective function and determined the search path by using the gradient descent, Newton, and advance-retreat methods.

2.2. Gradient-Descent Method. The direction of the partial derivative of the residual to the independent variable is taken as the search direction, and the first-order derivative of the updated objective function is close to zero [58, 59]. Combining the SWS with the gradient descent, we obtained the following equations of the objective function:

$$\begin{aligned} X &= [\theta, \Delta t]^T, \\ y &= f(X), \\ y_i &= f(X_i), \qquad (5) \\ \varphi &= \sum_{i=1}^{l} (y_i - m_i)^2. \end{aligned}$$
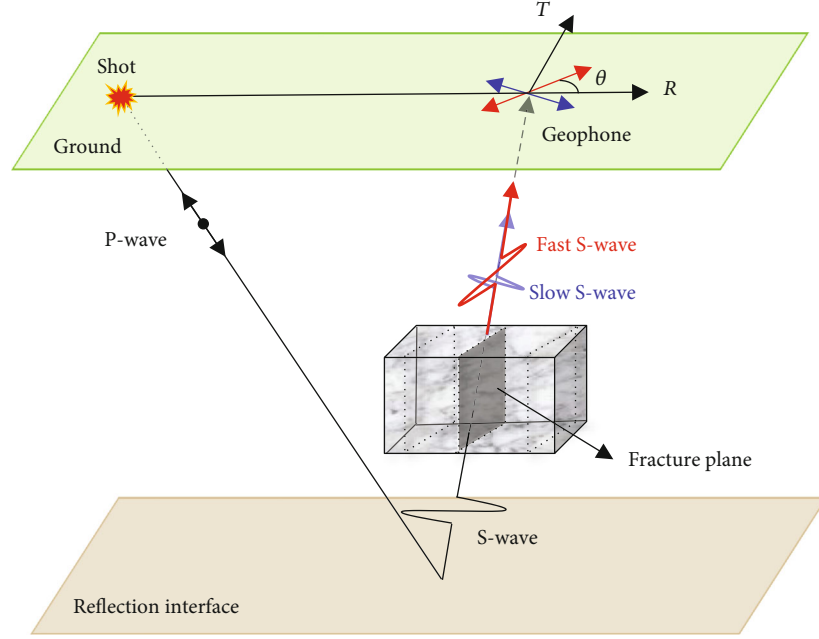
FIGURE 1: Shear-wave splitting (SWS) diagram. The red and blue arrows on the ground represent the polarization directions of the fast and slow shear waves, respectively, and θ represents the fracture azimuth.

We constructed model vector X with θ and Δt: the model value is y; f is the function rule between X and y; y_i is the ith model value; m_i is the ith observation value which always equals to 1; X_i is the ith parameter vector; the residual is φ of y_i and m_i; and l is the total number of observations.

The updates of the model value, residual, partial derivative, and vector X for the kth time can be written as

$$y^k = f\left(X^k\right),$$

$$\varphi^k = \sum_{i=1}^{l} \left(y_i^k - 1\right)^2,$$

$$\frac{\partial\left(\varphi^k\right)}{\partial(X)} = \left[\frac{\partial\left(\varphi^k\right)}{\partial(\theta)} \frac{\partial\left(\varphi^k\right)}{\partial(\Delta t)}\right]^T, \qquad (6)$$

$$X^k = \left[\theta^k, \Delta t^k\right]^T,$$

$$X^{k+1} = X^k - \alpha \times \frac{\partial\left(\varphi^k\right)}{\partial(X)},$$

where a is a step length. The update of SWS parameter θ and t can be written as follows:

$$\theta^{k+1} = \theta^k - \alpha \times \frac{\partial\left(\varphi^k\right)}{\partial(\theta)},$$

$$\Delta t^{k+1} = \Delta t^k - \alpha \times \frac{\partial\left(\varphi^k\right)}{\partial(\Delta t)}. \qquad (7)$$

However, we express the gradient value with a differential expression because the objective function is nonlinear. We obtained the four gradient values by differentiating the initial point (x_1, x_2) with its four adjacent grid points in the four directions of the binary function:

$$dF_1 = \frac{f(x_1 + \Delta x, x_2) - f(x_1, x_2)}{\Delta x},$$

$$dF_2 = \frac{f(x_1 - \Delta x, x_2) - f(x_1, x_2)}{-\Delta x},$$

$$dF_3 = \frac{f(x_1, x_2 + \Delta x) - f(x_1, x_2)}{\Delta x}, \qquad (8)$$

$$dF_4 = \frac{f(x_1, x_2 - \Delta x) - f(x_1, x_2)}{-\Delta x},$$

where dF_i is the gradient value, i represents the different directions, and Δx equals to 1. We take the adjacent point with the maximum value of dF_i as the update point. If the dF_i of the update point is less than ε_1 (a small positive number), the iteration is terminated and the corresponding θ and Δt of that point is the output.

We randomly selected an initial point on a surface to search for the optimal point (see Figure 2). After 14 iterations, we obtained the inversion result (optimal point).

2.3. Newton Method. The Newton method can quickly obtain the zero of the first-order derivatives of the objective function [60–62]. Based on the one-dimensional Newton
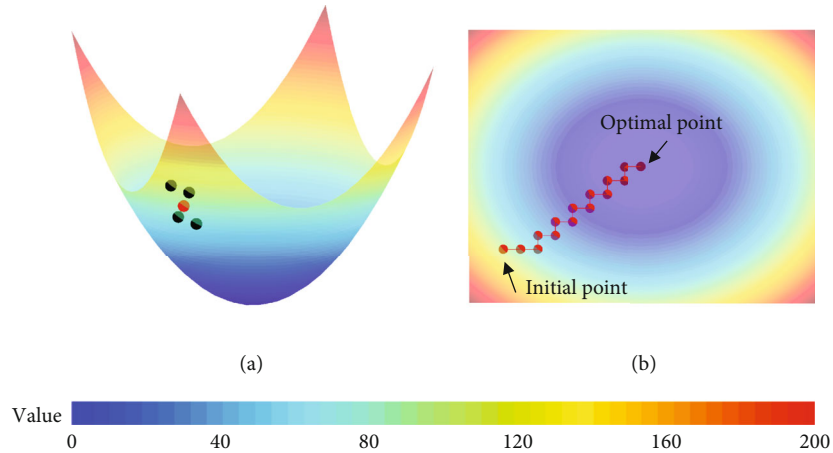
FIGURE 2: The convergence process of the gradient-descent method. (a) The red point is the initial point, and the black points are the adjacent points. (b) The convergence path. The extremum point is equal to the optimal value.
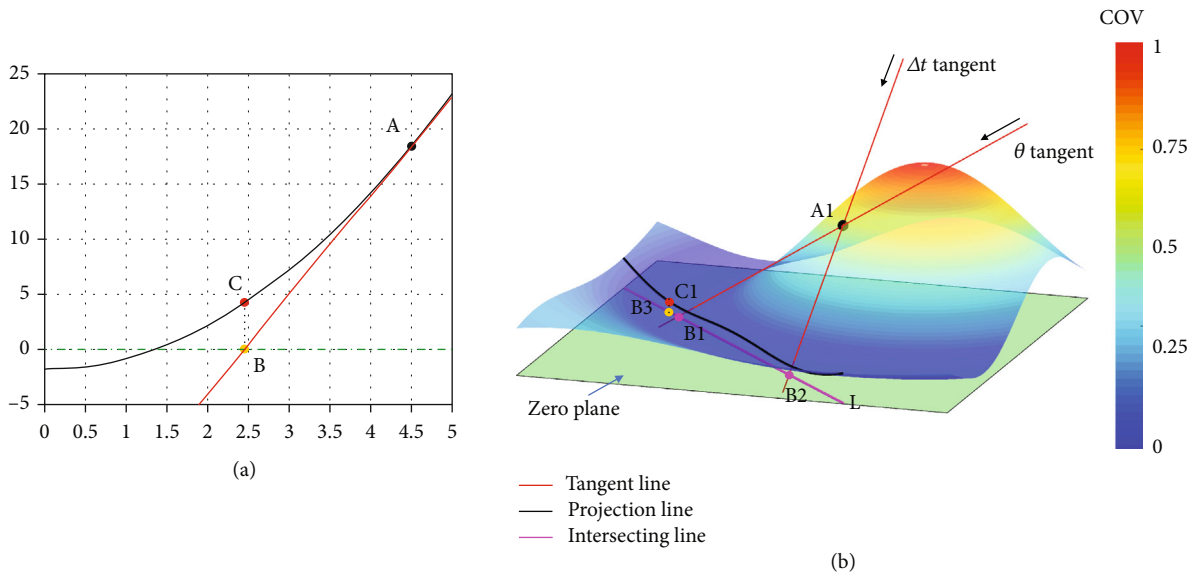

FIGURE 3: Convergence of the Newton method. (a) One-dimensional and (b) two-dimensional Newton methods.

method, the updates of vector X and SWS parameters θ and Δt can be calculated using

$$X^{k+1} = X^k - \frac{COV'}{COV''}, \quad COV' = \frac{\partial(COV)}{\partial(X)},$$

$$\theta^{k+1} = \theta^k - \frac{COV'_\theta}{COV''_\theta}, \quad COV'_\theta = \frac{\partial(COV)}{\partial(\theta)}, \qquad (9)$$

$$\Delta t^{k+1} = \Delta t^k - \frac{COV'_{\Delta t}}{COV''_{\Delta t}}, \quad COV'_{\Delta t} = \frac{\partial(COV)}{\partial(\Delta t)},$$

where COV' is the first-order derivative of the objective function and COV'' is the second-order derivative. The subscripts θ and Δt denote the partial derivatives of the

objective function for the azimuth or delay time direction, respectively.

The Newton method searches for zero through a tangent line (see Figure 3(a)). A is the initial point; B is the intersection point of the tangent and zero lines; and C is the projection of point B onto the objective function. The Newton method obtains the zero through the tangent line in one dimension and through the tangent plane in two dimensions. The tangent plane is composed of the θ and Δt tangents. The intersection points of tangent lines (θ and Δt) and the zero plane are points B1 and B2, respectively. The two points construct intersection line L. Then, computing the objective function values of all points on intersecting line L and comparing with each other, we can obtain C1 (the minimum COV'). B3, the projection point of C1 onto L, is the update point. We show the specific steps of the two-dimensional Newton method below (see Figure 3(b)).

We expressed the first-order derivative in differential form because the equation is nonlinear. The COV' value of the initial point $(\theta_1, \Delta t_1)$ is computed as

$$\text{COV}'(\theta_1, \Delta t_1) = \sqrt{\left(\frac{\text{COV}(\theta_1 + \Delta\theta, \Delta t_1) - \text{COV}(\theta_1, \Delta t_1)}{\Delta\theta}\right)^2 + \left(\frac{\text{COV}(\theta_1, \Delta t_1 + \Delta T) - \text{COV}(\theta_1, \Delta t_1)}{\Delta T}\right)^2}. \quad (10)$$

Then, we take points $(\theta_1 + \Delta\theta, \Delta t_1)$ and $(\theta_1, \Delta t_1 + \Delta T)$ as an increment in the azimuth and delay time directions, respectively. By substituting the two points into Equation (10), we can determine the first derivative of θ and Δt:

$$\text{COV}'_{\Delta\theta} = \text{COV}'(\theta_1 + \Delta\theta, \Delta t_1) = \sqrt{\left(\frac{\text{COV}(\theta_1 + 2\Delta\theta, \Delta t_1) - \text{COV}(\theta_1 + \Delta\theta, \Delta t_1)}{\Delta\theta}\right)^2 + \left(\frac{\text{COV}(\theta_1 + \Delta\theta, \Delta t_1 + \Delta T) - \text{COV}(\theta_1 + \Delta\theta, \Delta t_1)}{\Delta T}\right)^2}$$

$$\text{COV}'_{\Delta T} = \text{COV}'(\theta_1, \Delta t_1 + \Delta T) = \sqrt{\left(\frac{\text{COV}(\theta_1 + \Delta\theta, \Delta t_1 + \Delta T) - \text{COV}(\theta_1, \Delta t_1 + \Delta T)}{\Delta\theta}\right)^2 + \left(\frac{\text{COV}(\theta_1, \Delta t_1 + 2\Delta T) - \text{COV}(\theta_1, \Delta t_1 + \Delta T)}{\Delta T}\right)^2},$$

$$(11)$$

where $\text{COV}'_{\Delta\theta}$ and $\text{COV}'_{\Delta T}$ represent the values of the first-order derivative of the two points. Therefore, the tangent lines of the azimuth and delay time equations according to the $\text{COV}'_{\Delta\theta}$, $\text{COV}'_{\Delta T}$, and COV', can be written as

$$y_\theta = \frac{x - \theta_1}{\Delta\theta} \times \left(\text{COV}'_{\Delta\theta} - \text{COV}'\right) + \text{COV}',$$
$$y_{\Delta T} = \frac{x - \Delta t_1}{\Delta T} \times \left(\text{COV}'_{\Delta T} - \text{COV}'\right) + \text{COV}', \quad (12)$$

where y_θ and $y_{\Delta T}$ are the tangent lines of the azimuth and delay time, respectively, and x is the independent variable for azimuth or delay time.

We assumed that the COV' of point B1 is O_1 and B2 is O_2, and Z_1, Z_2, and Z_3 are substituted for COV', $\text{COV}'_{\Delta\theta}$, and $\text{COV}'_{\Delta T}$, respectively. Then, intersection points $B1(x_1, y_1, O_1)$ and $B2(x_2, y_2, O_2)$ can be calculated using O_1, O_2, Z_1, Z_2, and Z_3, which was expressed as

$$\frac{O_1 - Z_2}{Z_1 - Z_2} = \frac{x_1 - \theta_1 - \Delta\theta}{-\Delta\theta},$$
$$\frac{O_1 - Z_2}{Z_1 - Z_2} = \frac{y_1 - \Delta t_1}{\Delta t_1 - \Delta t_1},$$
$$\frac{O_2 - Z_3}{Z_1 - Z_3} = \frac{x_2 - \theta_1}{\theta_1 - \theta_1},$$
$$\frac{O_2 - Z_3}{Z_1 - Z_3} = \frac{y_2 - \Delta t_1 - \Delta T}{-\Delta T}. \quad (13)$$

Because O_1 and O_2 are equal to zero, Equation (13) can be simplified as

$$x_1 = \frac{\Delta\theta \times Z_2}{Z_1 - Z_2} + \theta_1 + \Delta\theta,$$
$$y_1 = \Delta t_1,$$
$$x_2 = \theta_1, \quad (14)$$
$$y_2 = \frac{\Delta T \times Z_3}{Z_1 - Z_3} + \Delta t_1 + \Delta T.$$

Then, the intersecting line, $L(x, y)$, formed by B1 and B2 can be expressed as

$$y = \frac{(x - x_2) \times (y_1 - y_2)}{x_1 - x_2} + y_2. \quad (15)$$

If x is the azimuth, y is the delay time. Then, calculating the projection values of intersecting line L onto the surface, we can obtain the minimum value of C1, taking B3, which is the projection point of C1 onto L, as the update point. If C1 is less than ε_2 (a small positive number), we take the point as the result; otherwise, the update continues.

2.4. Advance-Retreat Method Based on the Golden Section. The advance-retreat method determines the range, including the maximum value, by the opposite sign of the upper and lower bounds [63, 64], and the golden section method obtains the maximum value by narrowing the range [65, 66]. Then, we can obtain the maximum value quickly by

$(\theta_k, \Delta t_k)$

$\Delta t_{k+1} = \Delta t_k + h \ (h \neq 0)$

$\Delta t_k = \Delta t_{k+1}$
$h \to 2\,h$

No

$COV'_{\Delta t}(\theta_k, \Delta t_k)$
$COV'_{\Delta t}(\theta_k, \Delta t_{k+1}) < 0$

Yes

The range of Δt maximum ($[\Delta t_k, \Delta t_{k+1}]$) obtained, and the points of l_t and u_t are determined
$l_t = \Delta t_k + 0.382\,(\Delta t_{k+1} - \Delta t_k)$
$u_t = \Delta t_k + 0.618\,(\Delta t_{k+1} - \Delta t_k)$

$\Delta t_k = l_t$

No

$|COV'_{\Delta t}(\theta_k, l_t)| - |COV'_{\Delta t}(\theta_k, u_t)| < \varepsilon_{\Delta t}$

No

$|COV'_{\Delta t}(\theta_k, l_t)| < |COV'_{\Delta t}(\theta_k, u_t)|$

Yes

Yes

$\Delta t = (l_t + u_t)/2$

$\Delta t_{k+1} = u_t$

$\theta_k = \theta$
$\Delta t_k = \Delta t$

$\theta_{k+1} = \theta_k + h \ (h \neq 0)$

$\theta_k = \theta_{k+1}$
$h \to 2\,h$

No

$COV'_{\theta}(\theta_k, \Delta t)$
$COV'_{\theta}(\theta_{k+1}, \Delta t) < 0$

Yes

The range of θ maximum ($[\theta_k, \theta_{k+1}]$) obtained, and the points of l_t and u_t are determined
$l_{\theta} = \theta_k + 0.382\,(\theta_{k+1} - \theta_k)$
$u_{\theta} = \theta_k + 0.618\,(\theta_{k+1} - \theta_k)$

$\theta_k = l_{\theta}$

No

$|COV'_{\theta}(l_{\theta}, \Delta t)| - |COV'_{\theta}(u_{\theta}, \Delta t)| < \varepsilon_{\theta}$

No

$|COV'_{\theta}(l_{\theta}, \Delta t)| < |COV'_{\theta}(u_{\theta}, \Delta t)|$

Yes

Yes

$\theta = (l_{\theta} + u_{\theta})/2$

$\theta_{k+1} = u_{\theta}$

No

$|COV'_{\theta}(\theta, \Delta t)| < \varepsilon_3$

Yes

$(\theta, \Delta t)$

The procedure of determining the maximum of Δt

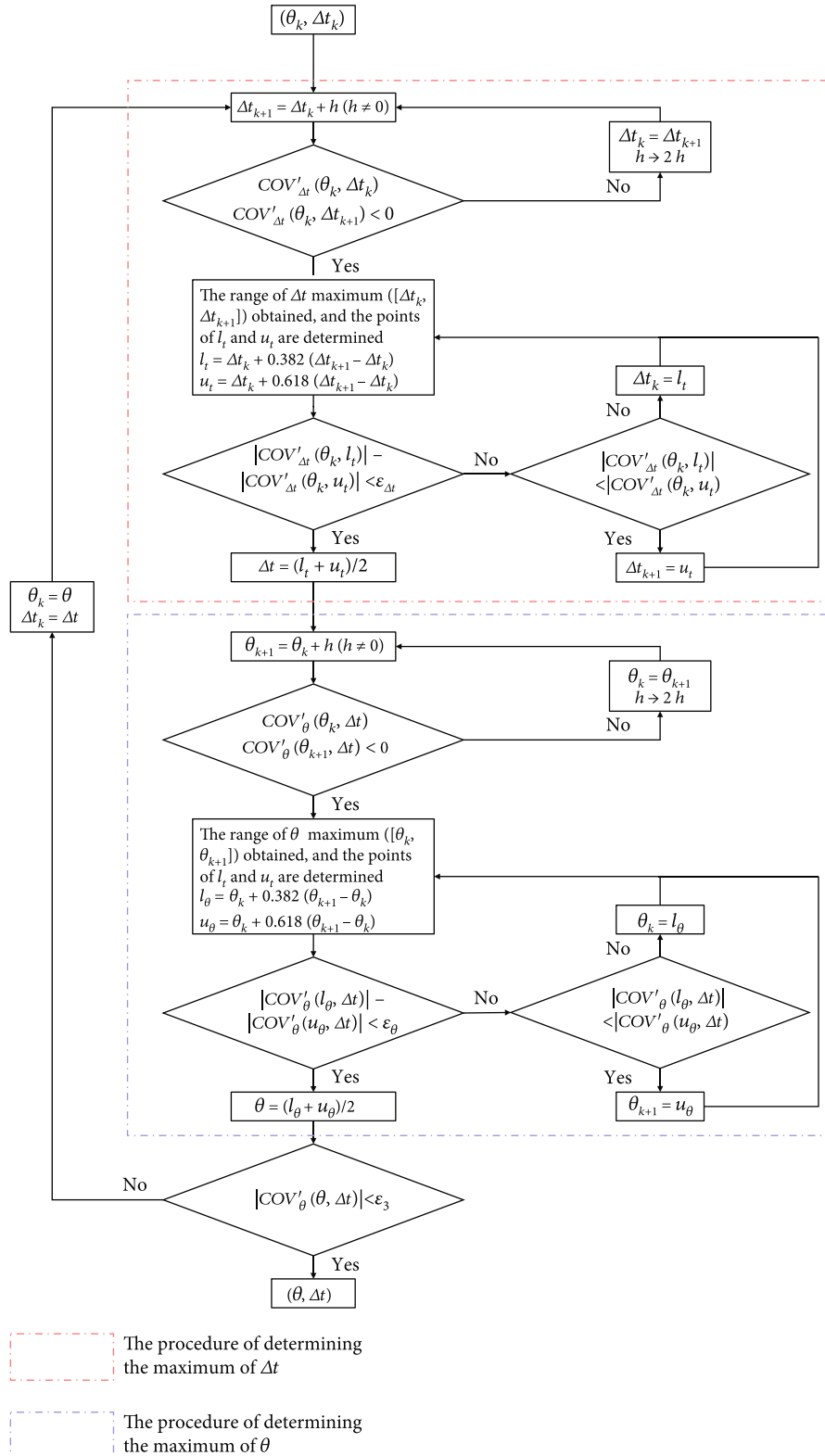The procedure of determining the maximum of θ

FIGURE 4: Flow chart of the advance-retreat method based on the golden section.

combining the two methods. The two-dimensional advance-retreat method obtains the maximum value of COV by regularly searching for the maximum value of the independent variables. This pattern searches for the maximum value in one direction and then continues to search for the maximum value in another direction. We output the point of the second maximum value as the result. If the COV' of the result is less than ε_3 (a small number), the loop is ended; otherwise,
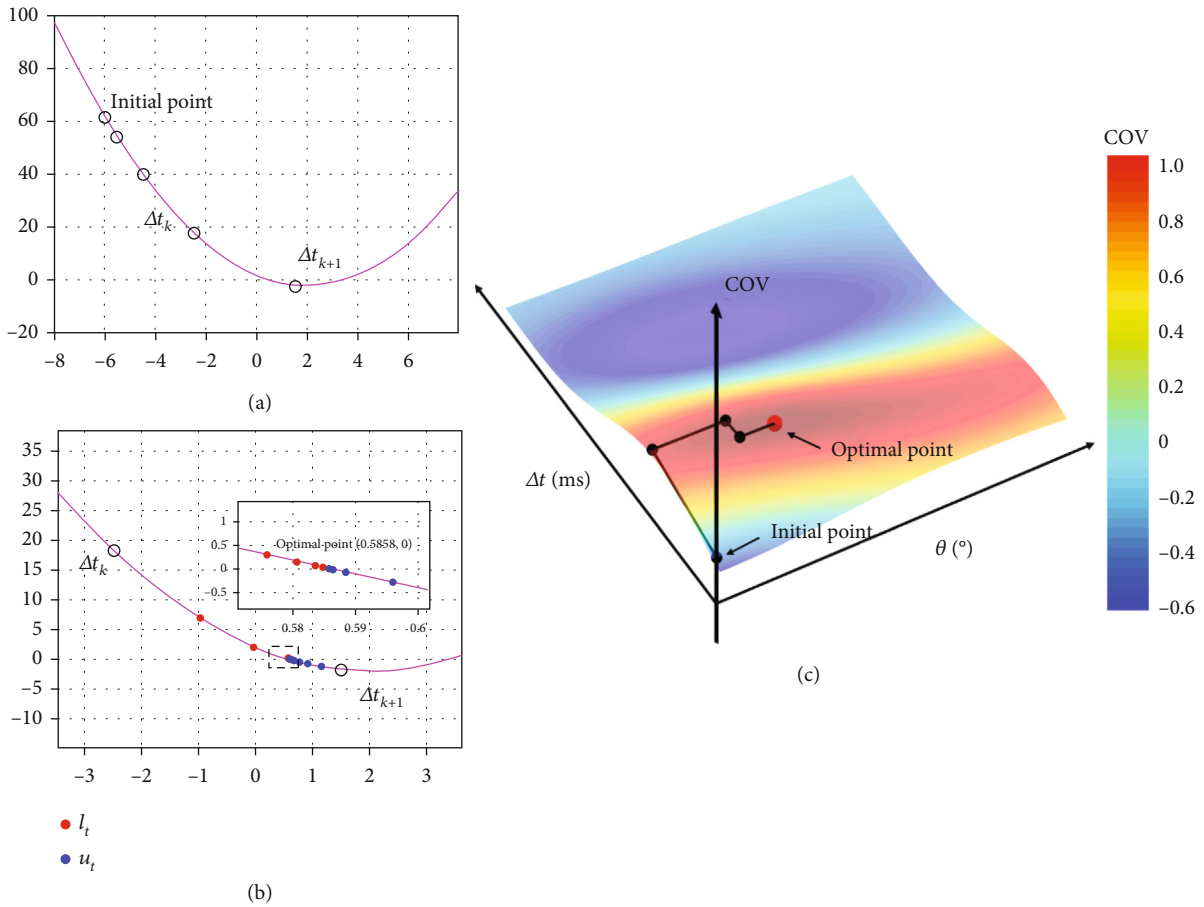
FIGURE 5: The search process of the advance and retreat method and simulation to find the real value of SWS. (a) One-dimensional advance-retreat method to find the range of maximum value $(\Delta t_k, \Delta t_{k+1})$. (b) The zero point (optimal point) is determined by narrowing the range. (c) The black points are the update points, and the red point is the real value.

advance-retreat is performed until the result satisfies the condition (COV′ less than the ε_3). We set the search pattern Δt to θ.

When searching for the maximum value of Δt, first, we must determine the range, including the maximum value of Δt. The range is determined by the values of the upper and lower bounds, which we use as the COV′ of the initial point $(\theta_k, \Delta t_k)$ and comparison point $(\theta_k, \Delta t_{k+1})$, respectively. The Δt_{k+1} equals Δt_k plus a step length h. Comparing whether $COV'_{\Delta t}(\theta_k, \Delta t_k)$ times $COV'_{\Delta t}(\theta_k, \Delta t_{k+1})$ is less than zero, we obtained the range $[\Delta t_k, \Delta t_{k+1}]$. If it is less than zero, we move to the next step. Otherwise, we obtained the new Δt_{k+1} which equals the new Δt_k plus the new h. The new Δt_k equals the last Δt_{k+1} and the new h is twice the last h. Then, we calculate the new $COV'_{\Delta t}(\theta_k, \Delta t_k)$ and $COV'_{\Delta t}(\theta_k, \Delta t_{k+1})$ to compare their signs. According to the sign, we choose to execute the golden section or continue to update the two points. The selection of this process is shown

$$COV'_{\Delta t}(\theta_k, \Delta t_k)COV'_{\Delta t}(\theta_k, \Delta t_{k+1}) > 0,$$

$$\Delta t_k = \Delta t_{k+1},$$

$$h \longrightarrow 2h,$$

$$\Delta t_{k+1} = \Delta t_k + h,$$

$$COV'_{\Delta t}(\theta_k, \Delta t_k)COV'_{\Delta t}(\theta_k, \Delta t_{k+1}) < 0,$$

$$\Delta t \in [\Delta t_k, \Delta t_{k+1}].$$

$$(16)$$

The second step is to narrow the range. Two comparison points (θ_k, l_t) and (θ_k, u_t) are determined, and l_t equals to Δt_k plus 0.382 times the difference between Δt_{k+1} and Δt_k. u_t equals Δt_k plus 0.618 times the difference between Δt_{k+1} and Δt_k, as shown in

$$l_t = \Delta t_k + 0.382 \times (\Delta t_{k+1} - \Delta t_k), \quad (17a)$$

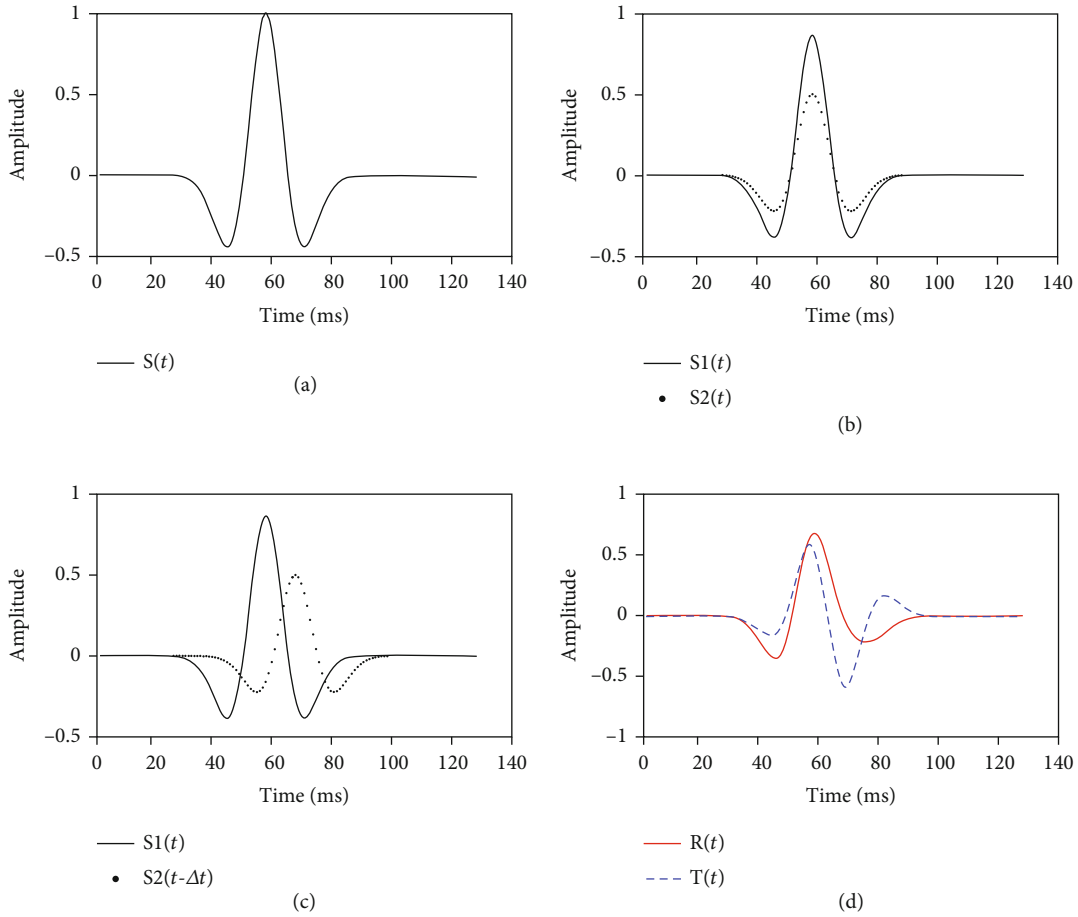$$u_t = \Delta t_k + 0.618 \times (\Delta t_{k+1} - \Delta t_k), \quad (17b)$$

FIGURE 6: Component signal time series. (a) Ricker wavelet $S(t)$, (b) fast shear wave $S1(t)$ and slow shear wave without delay $S2(t)$, (c) fast shear wave $S1(t)$ and slow shear wave $S2(t-\Delta t)$, and (d) R and T component time series.

Then, by comparing $|\mathrm{COV}_{\Delta t}'(\theta_k, l_t)|$ with $|\mathrm{COV}_{\Delta t}'(\theta_k, u_t)|$, we update l_t or u_t based on

$$
\begin{aligned}
&\left|\mathrm{COV}_{\Delta t}'(\theta_k, l_t)\right| > \left|\mathrm{COV}_{\Delta t}'(\theta_k, u_t)\right|, \\
&\qquad \Delta t_k = l_t, \\
&\qquad l_{t+1} = \Delta t_k + 0.382 \times (\Delta t_{k+1} - \Delta t_k),
\end{aligned}
\tag{18a}
$$

$$
\begin{aligned}
&\left|COV_{\Delta t}'(\theta_k, l_t)\right| < \left|\mathrm{COV}_{\Delta t}'(\theta_k, u_t)\right|, \\
&\qquad \Delta t_{k+1} = u_t, \\
&\qquad u_{t+1} = \Delta t_k + 0.618 \times (\Delta t_{k+1} - \Delta t_k),
\end{aligned}
\tag{18b}
$$

The update continues until the difference between $|\mathrm{COV}_{\Delta t}'(\theta_k, l_t)|$ and $|\mathrm{COV}_{\Delta t}'(\theta_k, u_t)|$ is less than precision $\varepsilon_{\Delta t}$ (a small positive number). Then, we obtain the maximum value of Δt which equals the sum of l_t plus u_t divided by 2.

This completes the search for the maximum value of Δt. The next step is to search for the maximum value of θ from the point $(\theta_k, \Delta t)$. The maximum value update process of θ is similar to the search for the maximum value of Δt. We obtained the comparison point $(\theta_{k+1}, \Delta t)$ using the initial point $(\theta_k, \Delta t)$, which is θ_{k+1}, equal to the θ_k plus step length h (a new step length). Then, we compared the sign of CO

$V_\theta'(\theta_k, \Delta t)$ with $\mathrm{COV}_\theta'(\theta_{k+1}, \Delta t)$ to choose to move onto the next step or update the two points. If it is different, the range is $[\theta_k, \theta_{k+1}]$; otherwise, we obtain the new θ_{k+1} which equals the new θ_k plus a new h (not h in the direction of the delay time), and the new θ_k equals the last θ_{k+1}, and the new h is twice the last h. Then, we calculate the new $\mathrm{COV}_\theta'(\theta_k, \Delta t)$ and $\mathrm{COV}_\theta'(\theta_{k+1}, \Delta t)$ to compare. The selection of this process is shown as

$$
\begin{aligned}
&COV_\theta'(\theta_k, \Delta t)COV_\theta'(\theta_{k+1}, \Delta t) > 0, \\
&\qquad\qquad \theta_k = \theta_{k+1}, \\
&\qquad\qquad h \longrightarrow 2h, \\
&\qquad\qquad \theta_{k+1} = \theta_k + h, \\
&COV_\theta'(\theta_k, \Delta t)COV_\theta'(\theta_{k+1}, \Delta t) < 0, \\
&\qquad\qquad \theta \in [\theta_k, \theta_{k+1}],
\end{aligned}
\tag{19}
$$

Then, we obtain l_θ and u_θ using

$$
l_\theta = \theta_k + 0.382 \times (\theta_{k+1} - \theta_k), \tag{20a}
$$

$$
u_\theta = \theta_k + 0.618 \times (\theta_{k+1} - \theta_k). \tag{20b}
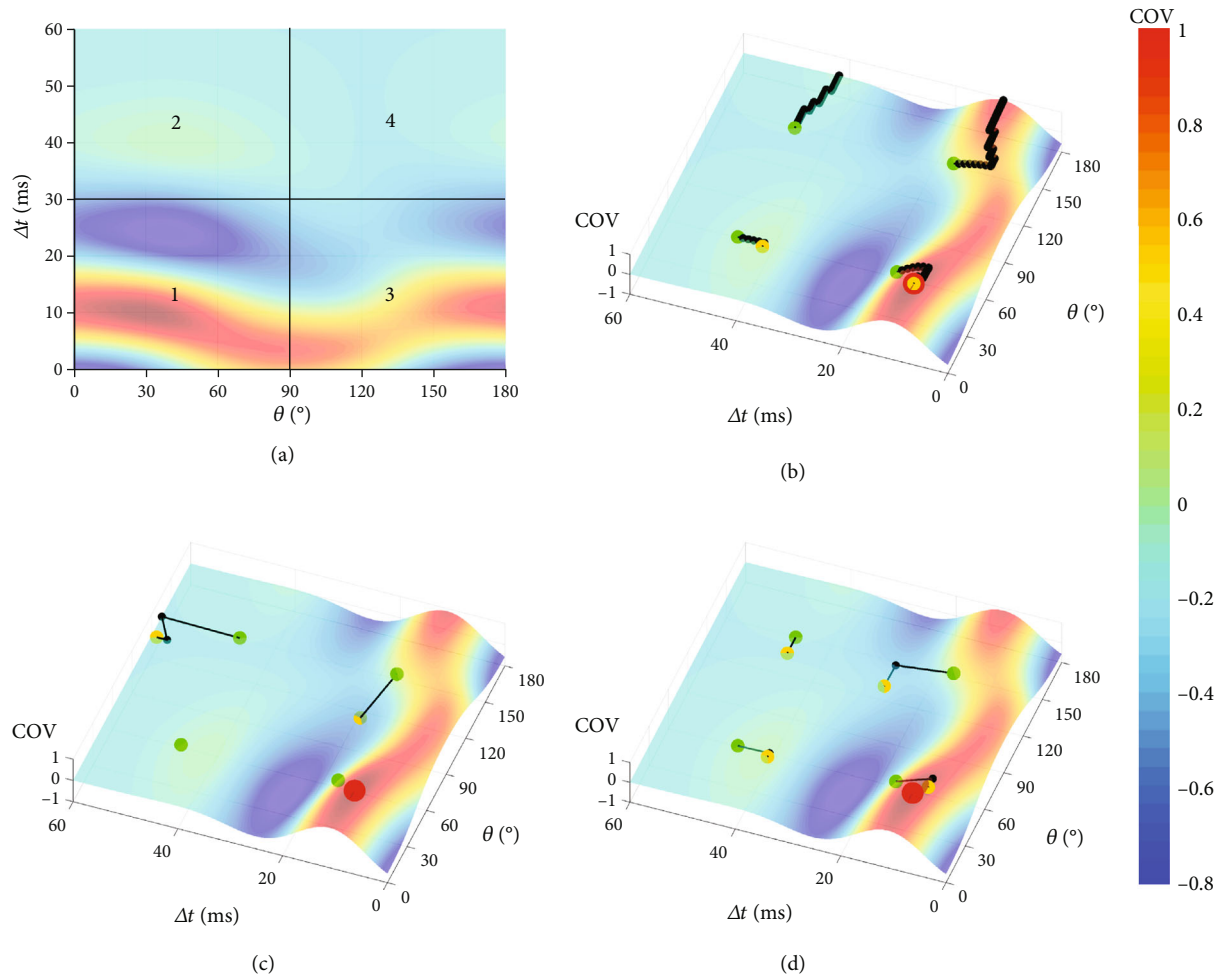$$

FIGURE 7: Diagram of the division and iterative process for the three methods. The red points are the real value (30, 10), the green points are the initial point, the black points are the update points, and the yellow points are the results for the subregion. (a) The divisions of the four subregions; the convergence process of the (b) gradient-descent method, (c) Newton method, and (d) advance-retreat method.

TABLE 1: Divisions and initial points of the four subregions.

	Subregion 1	Subregion 2	Subregion 3	Subregion 4
Azimuth region (°)	[0–90)	[0–90)	[90–180]	[90–180]
Delay time region (ms)	[0–30)	[30–60]	[0–30)	[30–60]
Initial point (°, ms)	(45,15)	(45,45)	(135,15)	(135,45)

Then, comparing the values of $|COV'_\theta(l_\theta, \Delta t)|$ with $|COV'_\theta(u_\theta, \Delta t)|$, we update l_θ or u_θ using

$$|COV'_\theta(l_\theta, \Delta t)| > |COV'_\theta(u_\theta, \Delta t)|,$$
$$\theta_k = l_\theta,$$ (21a)

$$l_{\theta+1} = \theta_k + 0.382 \times (\theta_{k+1} - \theta_k),$$
$$|COV'_\theta(l_\theta, \Delta t)| < |COV'_\theta(u_\theta, \Delta t)|,$$ (21b)
$$\theta_{k+1} = u_\theta,$$
$$u_{\theta+1} = \theta_k + 0.618 \times (\theta_{k+1} - \theta_k).$$

The iteration continues until the difference between $|COV'_\theta(l_\theta, \Delta t)|$ and $|COV'_\theta(u_\theta, \Delta t)|$ is less than precision ε_θ (a small positive number). The maximum value of θ equals the sum of l_θ plus u_θ divided by 2.

Then, we compute the COV' of the point $(\theta, \Delta t)$. If COV' is less than the precision ε_3 (a small positive number), we stop the loop and take the point as the result. Otherwise, the procedure continues to alternately search for the maximum values of Δt and θ until the COV' is less than ε_θ. The entire flowchart is shown in Figure 4.

If a point can be used in both positive and negative directions to search for the maximum value of Δt or θ, we need to calculate the maximum values of the two directions

TABLE 2: Calculation times and inversion results of the four methods.

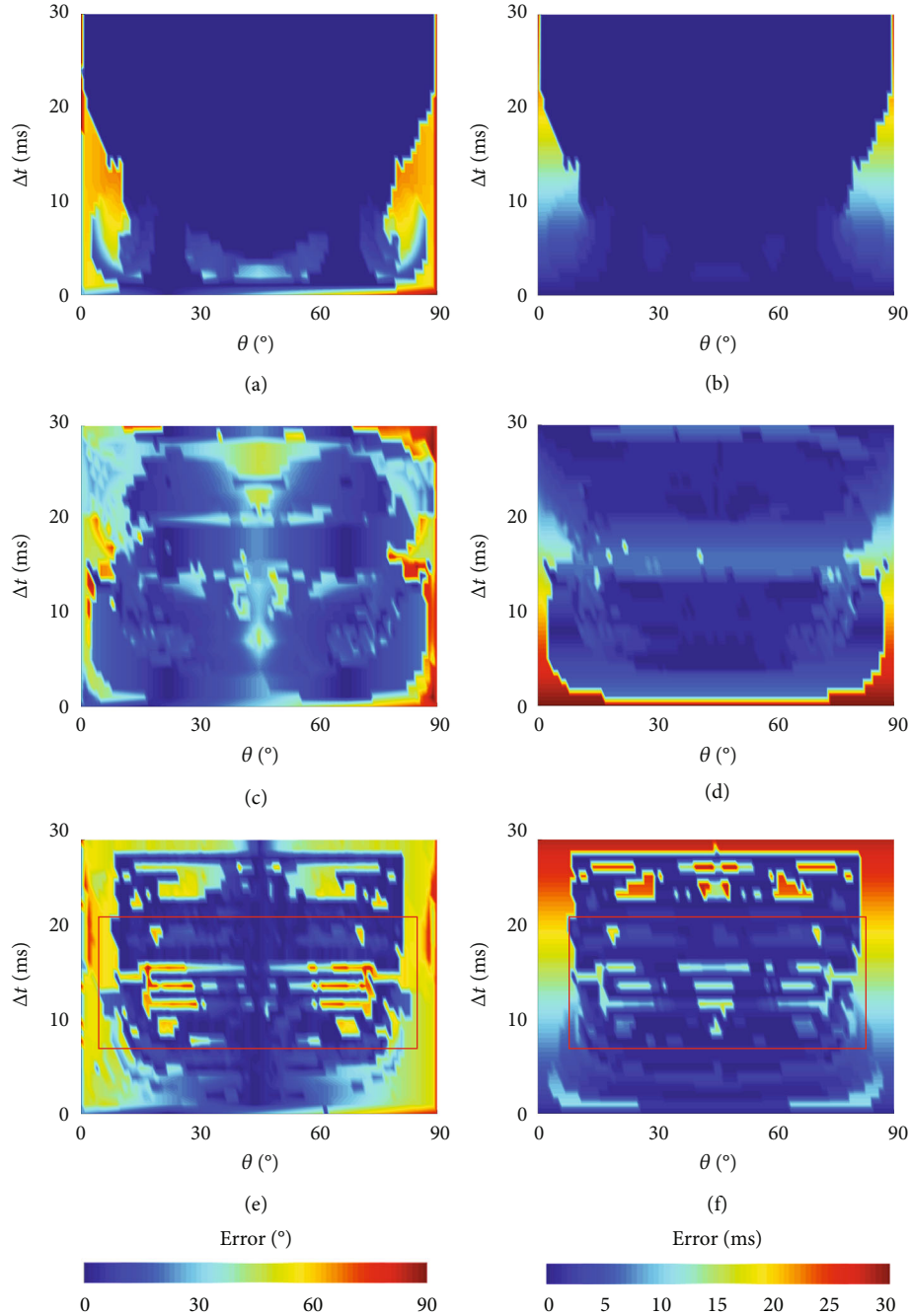|	Gradient descent	Newton	Advance-retreat	Rotation-correlation
Calculation times	191	218	69	11041
Result (°, ms)	(30,10)	(45,15)	(38,8)	(30,10)

FIGURE 8: Error comparison of the three methods. The left column is the azimuth error diagram and the right column is the delay time error diagram; (a, b) gradient-descent method, (c, d) Newton method, and (e, f) advance-retreat method.

and select the lower COV$'$ as the update point. Figures 5(a) and 5(b) show the advance-retreat method to find the maximum value in one dimension. Figure 5(a) shows how to quickly determine the range of maximum value as h

increases, and Figure 5(b) shows that the maximum value is obtained based on the golden section by narrowing its range. In Figure 5(c), we combined the SWS analysis with advance-retreat method to search for the real value. First,
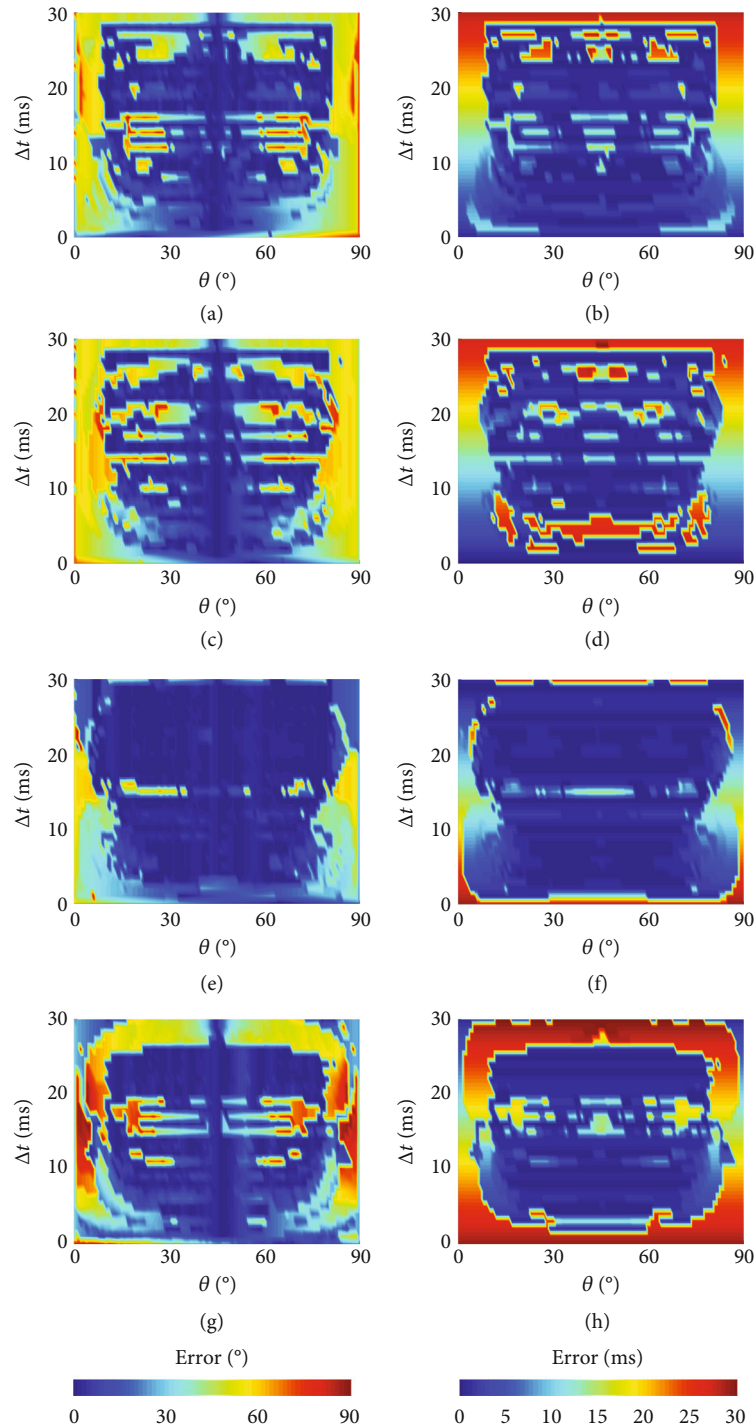
FIGURE 9: Error diagrams for the advance-retreat method with different initial step length; the left column is for the azimuth and the right column depicts delay time. The step length units from top to bottom are 1, 2, 3, and 4.

the zero point of the delay time is obtained, followed by the azimuth. The real value can be obtained after 4 iterations.

3. Synthetic Data Test

We compared the inversion results of the three methods through synthetic data. We used a Ricker wavelet (S) with a main frequency of 30 Hz to obtain the synthetic R and T component data. Δt and θ were set as 10 ms and 30°, respectively. The time window was set at 128 ms $S1(t)$ and $S2(t-\Delta t)$ were obtained using Equation (1), and $R(t)$ and $T(t)$ were obtained using Equation (2). The signal time series are as shown in Figure 6.

We set ε_1, ε_2, and ε_3 equal to 10^{-8}, $\varepsilon_{\Delta t}$ and ε_θ equal to 10^{-6}, and the step lengths of Δt and θ as 1° and 1 ms, respectively. The size of test region was set as 180×60, where 180 and 60
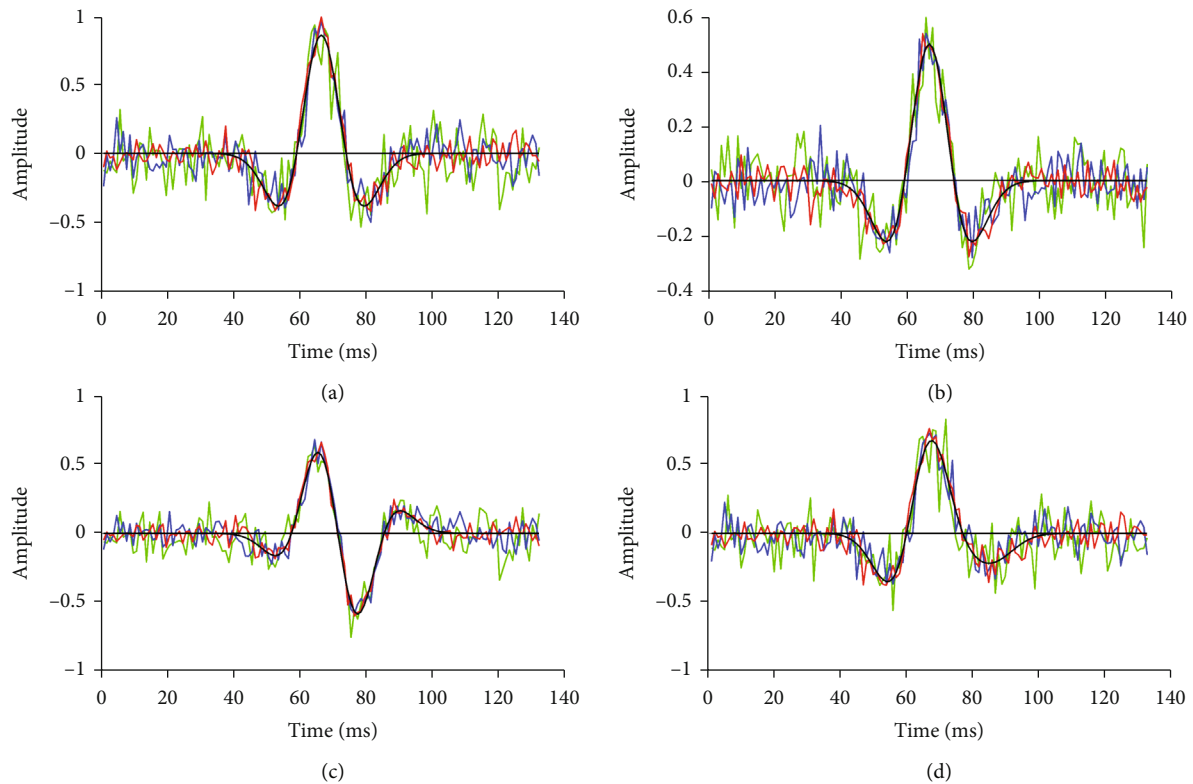
FIGURE 10: Original and noise-added signals. The black line represents the original signal, and the red, blue, and green lines represent the signals with 10%, 20%, and 50% noise level, respectively. (a) $S1(t)$ component time series, (b) $S2(t)$ component time series, (c) $T(t)$ component time series, and (d) $R(t)$ component time series.

are the ranges of the azimuth and delay time, respectively. The three methods may fall into the local convergence [67, 68]; therefore, to exclude local optima, we divided the region into four subregions and ran the computations in each subregion to obtain four output points. The maximum value is selected by comparing the four output points. The size of each subregion was 90×30, with a total of 2821 grid points (Figure 7(a)). Then, we took the central point of each subregion as the initial point. The SWS parameters corresponding to the maximum value of COV were obtained by comparing the output values of the four subregions. The subregions and initial points of the model are listed in Table 1, and Figure 7 shows the convergence progress of the three methods.

The calculation results and times for the three methods and the rotation-correlation method are shown in Table 2. The convergence speed of the three methods is all faster than the rotation-correlation method which requires 11,041 calculation times. Although the advance-retreat method had the least number of iterations, it cannot obtain accurate results. The gradient-descent method had the most accurate results.

We tested the inversion results of the three methods for 2,821 real values ranging from 0–90° and 0–30 ms with an increment of 1 unit to compare the errors of the three methods. The errors between the real values and results for the three methods are shown in Figure 8.

If the real azimuth was close to 0° or 90°, the errors of the three methods were high. When the azimuth was tilted to

15° to 75°, the inversion results of the gradient-descent method were the best with errors close to 0. As the delay time approached 15 ms, the error between the azimuth of inversion and the real value of the Newton method reached 30°. When the delay time was between 10 and 20 ms, the inversion results of the advance-retreat method displayed regular errors (see Figures 8(e) and 8(f), red box). The step length can affect the result of the advance-retreat method; therefore, to obtain the optimal step length, we compared the error diagram of the advance-retreat method with initial step length units of 1, 2, 3, and 4 (see Figure 9).

The comparison of the inversion method with different initial step lengths showed that when the azimuth ranged from 15–75°, the error of the inversion using a step length unit of 3 was close to 0, which was more accurate than other initial step units. Therefore, the initial step lengths of the advance-retreat method in the field data were set as 3° and 3 ms.

To test the stability of the gradient-descent method, we added 10%, 20%, and 50% noise level to the original signals $S1(t)$ and $S2(t)$ with azimuth and delay time of 30° and 10 ms, respectively. The time window of signals was 133 ms. We obtained the $R(t)$ and $T(t)$ with noise according to Equation (2) (Figure 10).

We tested the errors of the SWS analysis method combined with the gradient method and the rotation-correlation method for the noise-added signals. The delay time model was tested for 0–30 ms with an increment of 1 ms, and the
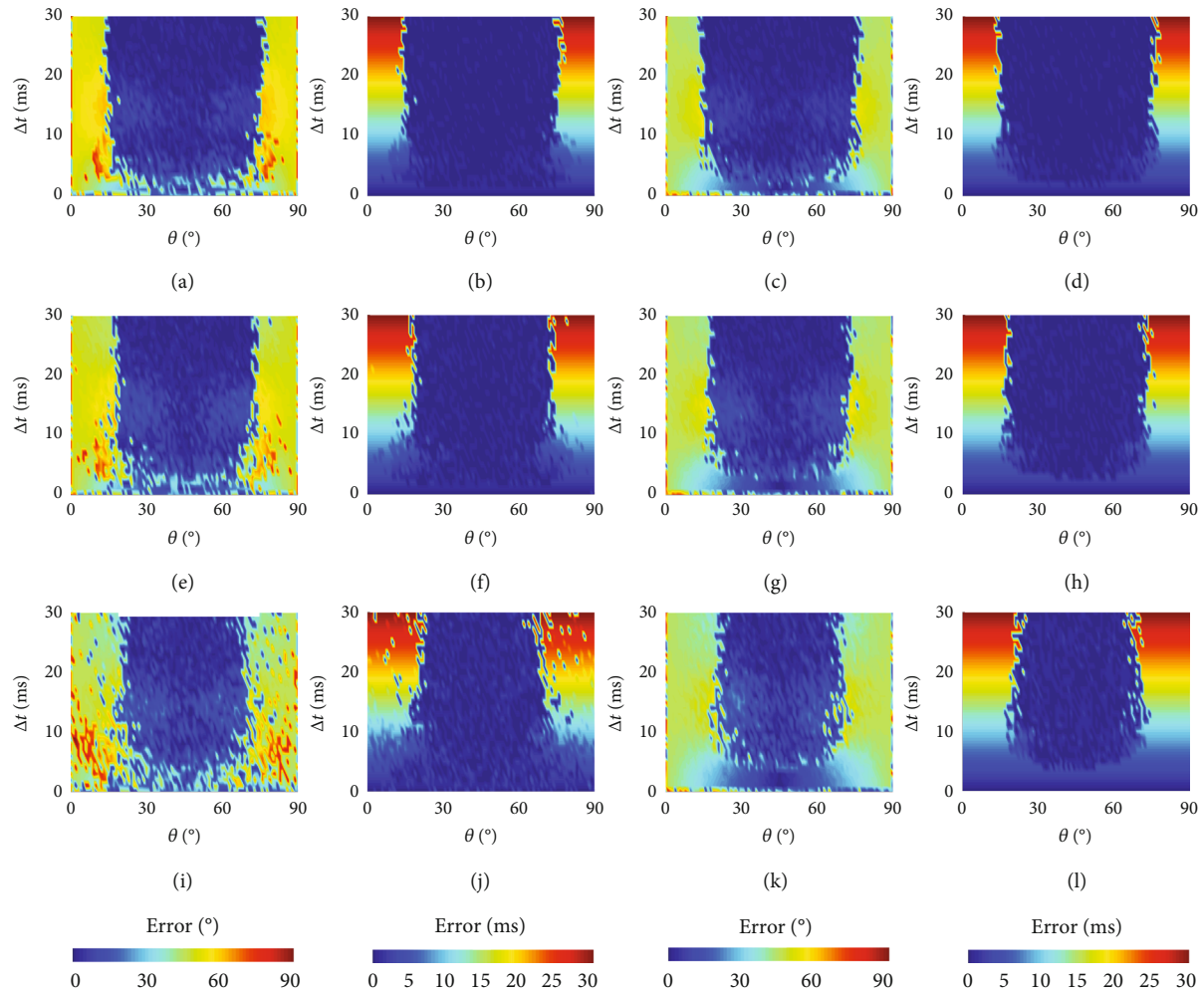
FIGURE 11: Error diagrams for the gradient method (first two columns on the left) and the rotation-correlation method (last two columns on the right). The first and third columns are the error diagrams for azimuth, and the second and fourth columns are the error diagrams for delay time. The noise levels from top to bottom are 10%, 20%, and 50%, respectively.

azimuth was tested for 0–90° with an increment of 1°. The error diagram is shown in Figure 11.

When the two methods are compared at the same noise level, the errors of azimuth and delay time are nearly similar. As the noise increases, the effective range of the azimuth narrows from 20–70° to 30–60°. Compared to the lower values of the delay time simulation (0–10 ms), the error of the gradient-descent method is smaller than the rotation-correlation method.

4. Field Data Testing

To verify the accuracy of the three methods, we used the R and T components of the field data to predict the degree of anisotropy and fracture azimuth of well A in Basin B, China. The target reservoir is a typical tight gas reservoir, and the prediction of fracture azimuths was key for improving productivity. The sections of R and T components are shown in Figure 12; well A is near the 50th trace. The target layer is the S Formation (see Figure 12, green dotted box). There-

fore, we selected the 50th trace of the R and T components to predict the anisotropic strength by using the three methods.

To ensure a complete wave mode in the time window and reduce the extent of unnecessary calculation, we set the length of the time window to be approximately one wavelength. We observed that the two adjacent wave peaks in the R or T components were close to 32 ms (see Figure 12). Therefore, the length of the time window was set as 32 ms. The subregion and initial point are shown in Table 3. We set the ratio of the delay and travel time in the target layer as the degree of anisotropy and fracture development. The presence of fractures caused changes in porosity, resulting in further changes in deep and shallow lateral resistivities [69]. Therefore, the fracture porosity can be calculated using these resistivities [70] as

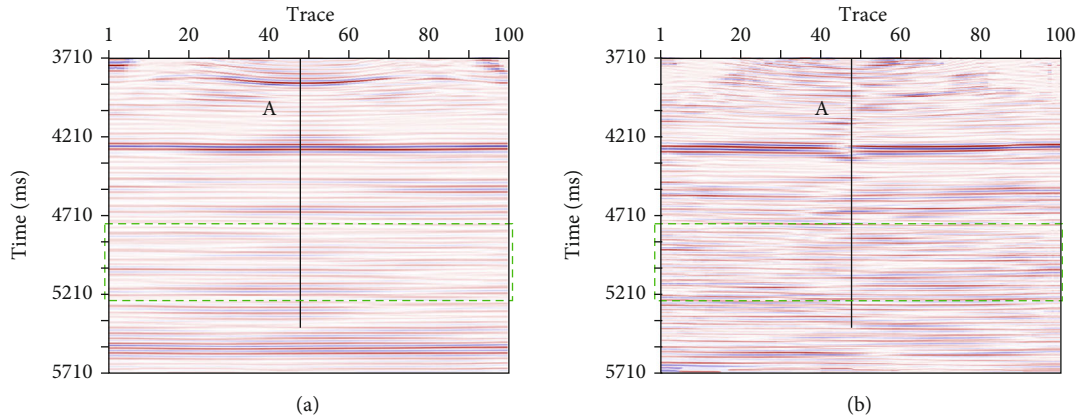$$\Phi_f = \left(\frac{A_1}{R_s} + \frac{A_2}{R_d} + A_3 \right) \times R_{mf}, \qquad (22)$$

FIGURE 12: R and T profiles of traces 1 to 100; the black line is well A. (a) R component profile and (b) T component profile.

TABLE 3: Divisions and initial points of the four subregions.

	Subregion 1	Subregion 2	Subregion 3	Subregion 4
Azimuth region (°)	[0–90]	[0–90]	[90–180]	[90–180]
Delay time region (ms)	[0–16]	[16–32]	[0–16]	[16–32]
Initial point (°, ms)	(45,8)	(45,24)	(135,8)	(135,24)

where R_s and R_d are the shallow and deep lateral resistivities, respectively; R_{mf} is resistivity of the mud filtrate; A_1, A_2, and A_3 are constants based on the statistical results from the same geologic age strata in the adjacent areas of basin B from oil field C. The constant values of the adjacent strata in Tarim Basin are $A_1 = -0.4063$, $A_2 = 1.2813$, and $A_3 = 0.000151$.

The curves of the fracture porosity and the results of rotation-correlation and the three methods are shown in Figure 13. The results of the gradient-descent method matched the fracture porosity curve best, especially between the depths of 6200–6290 and 6420–6480 m, as highlighted in the blue dotted boxes. The gradient-descent method required a maximum of 400 iterations, the maximum number of iterations for the advance-retreat method did not exceed 200, and the maximum number of iterations for the Newton method did not exceed 1200. The statistical results of calculation times showed that the gradient-descent method was calculated 75194 times in all depth locations, the Newton method 312356 times, the advance-retreat method 25192 times, and the rotation-correlation method 3153744 times. This shows that the gradient-descent method and the advance-retreat method can reduce the computation load by two orders of magnitude, while the Newton method can only reduce the computation load by one order of magnitude.

The other SWS parameter is the azimuth of the fast shear wave. We calculated the azimuths through the gradient-descent method and use a rose diagram (see Figure 14) to present the fracture azimuths. The dominant fracture azimuths in the target layer were distributed at approximately 45° and 135° (southwest–northeast and northwest–southeast). This result was consistent with that obtained by Yang et al. [71].

5. Discussion

Because grid search methods need to go through all the points to select the SWS parameters, the enumeration process involves a lot of unnecessary computation. In this study, we considered the COV (the objective function of rotation-correlation method) as the objective function. By setting an initial point, computational efficiency can be improved because the point can be updated autonomously toward the extremum point according to the theory of optimization algorithm.

The number of partitions is one of the parameters that can be adjusted in the three methods. Increasing the number of partitions will result in more output values, and the maximum value selected may be closer to the real value because there are more results to compare. However, an increase in the number of partitions necessarily increases computation times.

If the actual azimuth value is close to 0° or 90°, the results of these three methods are affected. Because the shear wave passes through the fractures almost parallel or orthogonal to the fracture plane, SWS does not occur—this is called the "null direction" [50]. The existence of a null measurement will result in constant $S1(t)$ and $S2(t)$ signals; therefore, according to Equation (5), the value of COV would be constant, and the gradient variation at any two adjacent points would be close to 0. Thus, the results of the SWS analysis are not accurate in this case.

The gradient-descent method was tested with Δx equal to 1. The convergence efficiency can be improved by setting different Δx, but this may affect the accuracy. In the future, we will consider setting Δx as a variable and not limiting the search direction to the positive and negative four directions in the xy axis. In addition, more search directions will be studied to achieve more effective results.
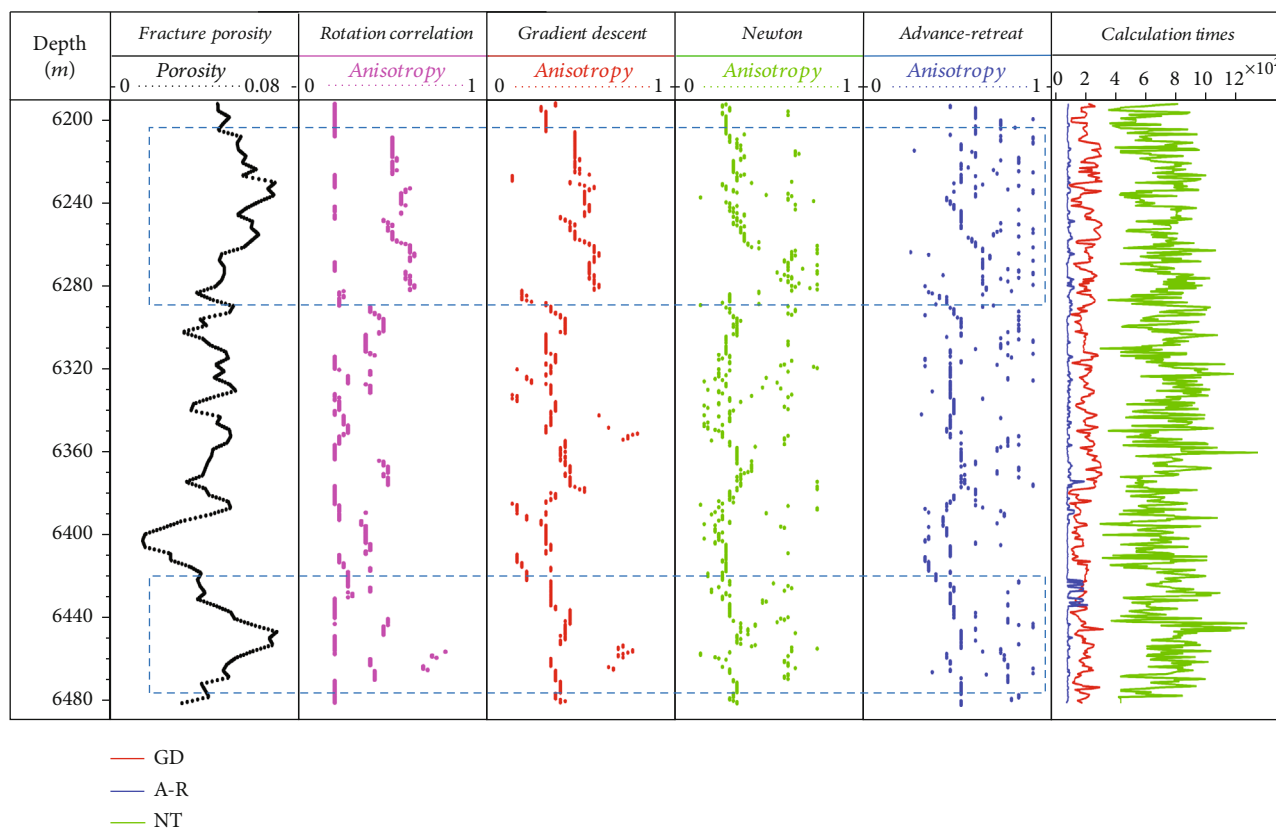
FIGURE 13: Comparison between the fracture prediction results from well-log analyses and the four methods. Track 1 shows the fracture porosity results based on the shallow and deep lateral resistivities; tracks 2–5 show the results of rotation-correlation and the three methods, respectively; and track 6 shows the calculation times of the three methods.
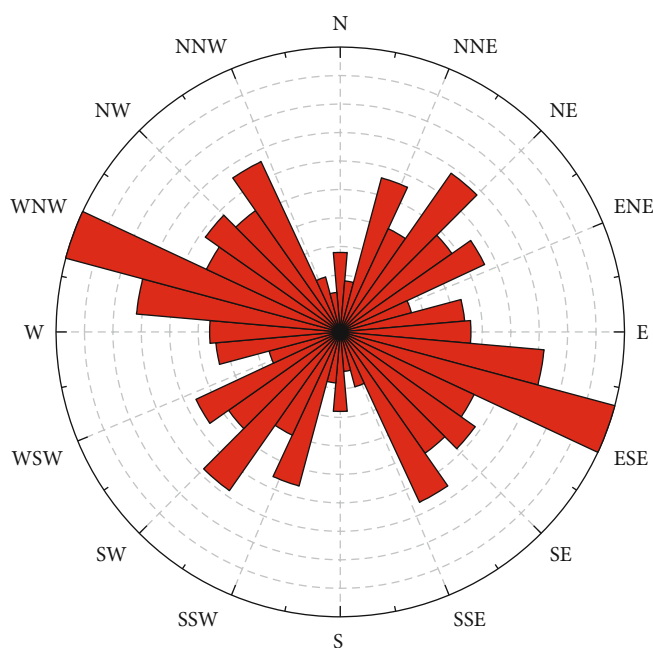

FIGURE 14: Fracture azimuth statistics for the gradient-descent method.

6. Conclusions

To improve the efficiency of the SWS analysis, we proposed new algorithms combining the gradient descent, Newton, and advance-retreat methods. We set the COV as the objective function, combined the characteristics of the three methods to guide the search path and selected the largest result by partitioning. The synthetic tests showed that the gradient-descent method is more accurate than the other two methods. The calculation times of the field data statistics show that the gradient descent and the advance-retreat methods can reduce the computation load by two orders of magnitude, while the Newton method can only reduce the computation load by one order of magnitude. The results predicted by the gradient-descent method are closer to the fracture porosity calculated by resistivity logging. The synthetic and field data tests both prove that the three methods are faster than traditional grid search methods, and that the gradient-descent method combined with SWS analysis is better than the other two methods. Our proposed SWS algorithm combined with the gradient-descent method can effectively improve the computational efficiency while the accuracy is guaranteed, and it can be applied for predicting the fracture azimuth and anisotropic strength in fractured reservoirs.

Data Availability

The original contributions presented in the study are included in the article; further inquiries can be directed to the corresponding author.

Conflicts of Interest

The authors declare that there is no conflict of interest regarding the publication of this paper.

Acknowledgments

References

[1] D. N. Espinoza, I. Shovkun, O. Makni, and N. Lenoir, "Natural and induced fractures in coal cores imaged through X-ray computed microtomography – impact on desorption time," *International Journal of Coal Geology*, vol. 154-155, pp. 165–175, 2016.

[2] Y. H. Li, Y. Song, Z. X. Jiang, L. S. Yin, M. Chen, and D. Liu, "Major factors controlling lamina induced fractures in the Upper Triassic Yanchang formation tight oil reservoir, Ordos Basin, China," *Journal of Asian Earth Sciences*, vol. 166, pp. 107–119, 2018.

[3] M. Widera, "Lignite cleat studies from the first Middle-Polish (first Lusatian) lignite seam in central Poland," *International Journal of Coal Geology*, vol. 131, pp. 227–238, 2014.

[4] S. Crampin, R. Evans, B. Üçer et al., "Observations of dilatancy-induced polarization anomalies and earthquake prediction," *Nature*, vol. 286, no. 5776, pp. 874–877, 1980.

[5] D. F. Winterstein and M. A. Meadows, "Shear-wave polarizations and subsurface stress directions at lost hills field," *Geophysics*, vol. 56, no. 9, pp. 1331–1348, 1991.

[6] D. F. Becker and A. I. Perelberg, "Seismic detection of subsurface fractures," *Geophysics*, vol. 52, no. 5, pp. 708-709, 1987.

[7] S. Crampin, "Shear wave polarizations: a plea for three-component recording," in *EG Technical Program Expanded Abstracts*, Las Vegas, Nevada, 1983.

[8] S. Crampin, "Seismic-wave propagation through a cracked solid: polarization as a possible dilatancy diagnostic," *Geophysical Journal International*, vol. 53, no. 3, pp. 467–496, 1978.

[9] D. Wang and B. Li, "Characterization of porous rocks embedded with aligned fractures from shear wave responses," *Geophysical Journal International*, vol. 222, no. 3, pp. 2172–2188, 2020.

[10] K. Kayama, H. Mikada, and J. Takekawa, "Dispersion of flexural waves in a borehole with a tensile fracture in an anisotropic stress environment," *Geophysical Prospecting*, vol. 69, no. 3, pp. 598–607, 2021.

[11] M. Adelinet, C. Dorbath, M. Calò, L. Dorbath, and M. Le Ravalec, "Crack features and shear-wave splitting associated with fracture extension during hydraulic stimulation of the geothermal reservoir in Soultz-sous-Forêts," *Oil and Gas Science and Technology*, vol. 71, no. 3, p. 39, 2016.

[12] E. Y. Jiang, K. H. Liu, Y. Gao, X. F. Fu, and S. S. Gao, "Spatial variations of upper crustal anisotropy along the San Jacinto fault zone in southern California: constraints from shear wave splitting analysis," *Journal of Geophysical Research-Solid Earth*, vol. 126, no. 4, pp. 1–13, 2021.

[13] X. M. Tang and R. K. Chunduru, "Simultaneous inversion of formation shear-wave anisotropy parameters from cross-dipole acoustic-array waveform data," *Geophysics*, vol. 64, no. 5, pp. 1502–1511, 1999.

[14] M. Li, G. Tao, H. Wang, K. Zhang, and S. Vega, "An improved multiscale and leaky P-wave removal analysis for shear-wave anisotropy inversion with crossed-dipole logs," *Petrophysics*, vol. 57, no. 3, pp. 270–293, 2016.

[15] G. Hein, P. Kolínský, I. Bianchi, G. Bokelmann, and AlpArray Working Group, "Shear wave splitting in the Alpine region," *Geophysical Journal International*, vol. 227, no. 3, pp. 1996–2015, 2021.

[16] E. Löberich, M. D. Long, L. S. Wanger, E. Qorbani, and G. Bokelmann, "Constraints on olivine deformation from SKS shear-wave splitting beneath the southern Cascadia subduction zone back-arc," *Geochemistry, Geophysics, Geosystems*, vol. 22, no. 11, pp. 1525–2027, 2021.

[17] R. M. Alford, "Shear data in the presence of azimuthal anisotropy: Dilley, Texas," *Geophysics*, vol. 52, no. 3, p. 424, 1986.

[18] M. A. Martin and T. L. Davis, "Shear-wave birefringence: a new tool for evaluating fractured reservoirs," *Geophysics: The Leading Edge of Exploration*, vol. 6, no. 10, pp. 22–28, 1987.

[19] X. Y. Li and S. Crampin, "Linear-transform techniques for processing shear-wave anisotropy in four-component seismic data," *Geophysics*, vol. 58, no. 2, pp. 240–256, 1993.

[20] X. Y. Li and C. MacBeth, "Data-matrix asymmetry and polarization changes from multicomponent surface seismics," *Geophysics*, vol. 62, no. 2, pp. 630–643, 1997.

[21] A. Benhama, C. Cliet, and M. Dubesset, "Study and applications of spatial directional filtering in three-component recordings1," *Geophysical Prospecting*, vol. 36, no. 6, pp. 591–613, 1988.

[22] M. Boulfoul and D. R. Watts, "Separation and enhancement of splitS-waves on multicomponent shot records from the BIRPS WISPA experiment," *Geophysics*, vol. 59, no. 1, pp. 131–139, 1994.

[23] L. Vecsey, J. Plomerová, and V. Babuška, "Shear-wave splitting measurements – problems and solutions," *Tectonophysics*, vol. 462, no. 1-4, pp. 178–196, 2008.

[24] H. Y. Shen and Q. C. Li, "Seismic wave field separation and noise attenuation in linear domain via SVD," in *Paper presented at SEG Annual Meeting*, Houston, Texas, 2009.

[25] L. P. Vinnik, R. Kind, G. L. Kosarev, and L. I. Makeyeva, "Azimuthal anisotropy in the lithosphere from observations of long-period S-waves," *Geophysical Journal International*, vol. 99, no. 3, pp. 549–559, 1989.

[26] X. B. Tian, J. L. Zhang, S. K. Si, J. B. Wang, Y. Chen, and Z. J. Zhang, "SKS splitting measurements with horizontal component misalignment," *Geophysical Journal International*, vol. 185, no. 1, pp. 329–340, 2011.

[27] T. Eken and F. Tilmann, "The use of direct shear waves in quantifying seismic anisotropy: exploiting regional arrays," *Bulletin of the Seismological Society of America*, vol. 104, no. 6, pp. 2644–2661, 2014.

[28] P. G. Silver and W. W. Chan, "Shear wave splitting and subcontinental mantle deformation," *Journal of Geophysical Research-Solid Earth*, vol. 96, no. B10, pp. 16429–16454, 1991.

[29] M. S. Diallo, M. Kulesh, M. Holschneider, K. Kurennaya, and F. Scherbaum, "Instantaneous polarization attributes based on an adaptive approximate covariance method," *Geophysics*, vol. 71, no. 5, pp. V99–V104, 2006.

[30] R. Robinson, A. Li, A. Savvaidis, and H. Hu, "Complex shear-wave anisotropy from induced earthquakes in West Texas," *Bulletin of the Seismological Society of America*, vol. 110, no. 5, pp. 2242–2251, 2020.

[31] M. Ando, Y. Ishikawa, and F. Yamazaki, "Shear wave polarization anisotropy in the upper mantle beneath Honshu, Japan," *Journal of Geophysical Research*, vol. 88, no. B7, pp. 5850–5864, 1983.

[32] Y. Fukao and Y. Tono, "Shear-wave splitting apparently caused by contamination of P-to-S or S-to-P converted waves," *Bulletin of the Seismological Society of America*, vol. 103, no. 2A, pp. 950–957, 2013.

[33] J. P. Grossman, G. Popov, and C. Steinhoff, "Integration of multicomponent time-lapse processing and interpretation: focus on shear-wave splitting analysis," *Leading Edge*, vol. 32, no. 1, pp. 32–38, 2013.

[34] M. Hodges and M. S. Miller, "Mantle flow at the highly arcuate northeast corner of the Lesser Antilles subduction zone: constraints from shear-wave splitting analyses," *Lithosphere*, vol. 7, no. 5, pp. 579–587, 2015.

[35] J. Lu, Y. Wang, J. Y. Chen, and Y. An, "Joint anisotropic amplitude variation with offset inversion of PP and PS seismic data," *Geophysics*, vol. 83, no. 2, pp. N31–N50, 2018.

[36] P. P. Moghaddam, H. Keers, F. J. Herrmann, and W. A. Mulder, "A new optimization approach for source-encoding full-waveform inversion," *Geophysics*, vol. 78, no. 3, pp. R125–R132, 2013.

[37] C. A. Xiao, H. S. Tang, Y. Ren, J. W. Xiang, and K. Anil, "Adaptive MOMEDA based on improved advance-retreat algorithm for fault features extraction of axial piston pump," *ISA Transactions*, vol. 10, p. 33, 2021.

[38] J. L. He, Y. Yang, H. C. Zhu, K. Li, W. Yao, and K. Huang, "Microwave heating based on two rotary waveguides to improve efficiency and uniformity by gradient descent method," *Applied Thermal Engineering*, vol. 178, article 115594, 2020.

[39] T. D. Niri, S. A. S. Fazeli, and M. Heydari, "A two-step improved Newton method to solve convex unconstrained optimization problems," *Journal of Applied Mathematics & Computing*, vol. 62, no. 1-2, pp. 37–53, 2020.

[40] L. Xue, X. Ling, and S. S. Yang, "Mechanical behaviour and strain rate sensitivity analysis of TA2 by the small punch test," *Theoretical and Applied Fracture Mechanics*, vol. 99, pp. 9–17, 2019.

[41] J. R. Bowman and M. Ando, "Shear-wave splitting in the upper-mantle wedge above the Tonga subduction zone," *Geophysical Journal International*, vol. 88, no. 1, pp. 25–41, 1987.

[42] K. Bhukta, A. Paul, and P. K. Khan, "SKS and SKKS splitting measurements beneath the NW Himalaya," *Pure and Applied Geophysics*, vol. 179, no. 2, pp. 641–661, 2022.

[43] K. Bhukta, P. K. Khan, and P. Mandal, "Upper mantle anisotropy inferred from shear wave splitting beneath the Eastern Indian Shield region," *Geoscience Frontiers*, vol. 9, no. 6, pp. 1911–1920, 2018.

[44] W. Gajek, D. Gräff, S. Hellmann, A. W. Rempel, and F. Walter, "Diurnal expansion and contraction of englacial fracture networks revealed by seismic shear wave splitting," *Communications Earth & Environment*, vol. 2, pp. 2662–4435, 2021.

[45] N. Uchida, J. Nakajima, K. Wang et al., "Stagnant forearc mantle wedge inferred from mapping of shear-wave anisotropy using S-net seafloor seismometers," *Nature Communications*, vol. 11, 2020.

[46] J. D. West, M. J. Fouch, J. B. Roth, and L. T. Elkins-Tanton, "Vertical mantle flow associated with a lithospheric drip beneath the Great Basin," *Nature Geoscience*, vol. 2, no. 6, pp. 439–444, 2009.

[47] M. Tsekhmistrenko, K. Sigloch, K. Hosseini, and G. Barruol, "A tree of Indo-African mantle plumes imaged by seismic tomography," *Nature Geoscience*, vol. 14, no. 8, pp. 612–619, 2021.

[48] I. Spingos, G. Kaviris, C. Millas, P. Papadimitriou, and N. Voulgaris, "Pytheas: an open-source software solution for local shear-wave splitting studies," *Computers & Geosciences*, vol. 134, article 104346, 2020.

[49] S. Biswal, S. Kumar, S. K. Roy et al., "Upper mantle anisotropy beneath the Western segment, NW Indian Himalaya, using shear wave splitting," *Lithosphere*, vol. 2020, article 8856812, no. 1, 2020.

[50] A. Wüstefeld and G. Bokelmann, "Null detection in shear-wave splitting measurements," *Bulletin of the Seismological Society of America*, vol. 97, no. 4, pp. 1204–1211, 2007.

[51] R. Bale, B. Gratacos, B. Mattocks, S. Roche, K. Poplavskii, and X. Li, "Shear wave splitting applications for fracture analysis and improved imaging: some onshore examples," *First Break*, vol. 27, no. 9, pp. 73–83, 2009.

[52] J. L. Zhang, Y. Wang, and J. Lu, "A new algorithm for frequency-dependent shear-wave splitting parameters

extraction," *Journal of Geophysics and Engineering*, vol. 10, no. 5, article 055005, 2013.

[53] M. Long and P. Silver, "Shear wave splitting and mantle anisotropy: measurements, interpretations, and new directions," *Surveys in Geophysics*, vol. 30, no. 4-5, pp. 407–461, 2009.

[54] F. Link, M. C. Reiss, and G. Rümpker, "An automated XKS-splitting procedure for large data sets: extension package for SplitRacer and application to the USArray," *Computers & Geosciences*, vol. 158, article 104961, 2022.

[55] A. T. Sasmi, A. D. Nugraha, M. Muzli et al., "Determination of shear wave splitting parameters in 2018 Lombok earthquake using rotation correlation method: preliminary result," *IOP Conference Series: Earth and Environmental Science*, vol. 873, article 012101, 2021.

[56] A. L. White-Gaynor and A. A. Nyblade, "Shear wave splitting across the Mid-Atlantic region of North America: a fossil anisotropy interpretation," *Geology*, vol. 45, no. 6, pp. 555–558, 2017.

[57] J. Acevedo, G. Fernández-Viejo, S. Llana-Fúnez, C. López-Fernández, and J. Olona, "Upper-crustal seismic anisotropy in the Cantabrian Mountains (North Spain) from shear-wave splitting and ambient noise interferometry analysis," *Seismological Research Letters*, vol. 92, no. 1, pp. 421–436, 2021.

[58] T. J. Hayes, K. F. Tiampo, J. Fernández, and J. B. Rundle, "A gravity gradient method for characterizing the post-seismic deformation field for a finite fault," *Geophysical Journal International*, vol. 173, no. 3, pp. 802–805, 2008.

[59] R. Rashetnia and M. Pour-Ghaz, "Deep learning surrogate interacting Markov chain Monte Carlo based full wave inversion scheme for properties of materials quantification," *Journal of Sound and Vibration*, vol. 497, article 115934, 2021.

[60] M. Monsalve and M. Raydan, "Newton's method and secant methods: a longstanding relationship from vectors to matrices," *Portugaliæ Mathematica*, vol. 68, no. 4, pp. 461–475, 2011.

[61] M. H. Loke and T. Dahlin, "A comparison of the Gauss-Newton and quasi-Newton methods in resistivity imaging inversion," *Journal of Applied Geophysics*, vol. 49, no. 3, pp. 149–162, 2002.

[62] R. Martínez-Planell, M. T. Gaismán, and D. McGee, "Students' understanding of the relation between tangent plane and directional derivatives of functions of two variables," *Journal of Mathematical Behavior*, vol. 46, pp. 13–41, 2017.

[63] H. P. Li, G. Q. Zhao, S. T. Niu, and Y. G. Luan, "Inverse heat conduction analysis of quenching process using finite-element and optimization method," *Finite Elements in Analysis and Design*, vol. 42, no. 12, pp. 1087–1096, 2006.

[64] K. Ma, Y. G. Bai, J. Yang, Y. Q. Yu, and Q. X. Yang, "Demand-side energy management based on nonconvex optimization in smart grid," *Energies*, vol. 10, no. 10, p. 1538, 2017.

[65] R. G. Sacco, "Fibonacci harmonics: a new mathematical model of synchronicity," *Applied Mathematics*, vol. 9, no. 6, pp. 702–718, 2018.

[66] E. Cuevas, L. Enríquez, D. Zaldívar, and M. Pérez-Cisneros, "A selection method for evolutionary algorithms based on the golden section," *Expert Systems with Applications*, vol. 106, pp. 183–196, 2018.

[67] R. Behl, I. K. Argyros, J. A. T. Machado, and A. S. Alshomrani, "Local convergence of a family of weighted-Newton methods," *Symmetry*, vol. 11, no. 1, p. 103, 2019.

[68] A. Aurasopon and W. Khamsen, "An improved local search involving bee colony optimization using lambda iteration combined with a golden section search method to solve an economic dispatch problem," *Przeglad Elektrothchniczny*, vol. 95, no. 1, pp. 202–208, 2019.

[69] A. M. Sibbit and O. Faivre, "The dual laterolog response in fractured rocks," in *SPWLA 26th Annual Logging Symposium*, pp. 1–31, Dallas, Texas, 1985.

[70] S. J. Li, C. W. Xiao, H. M. Wang, and G. J. Zhang, "Mathematical model of dual laterolog response to fracture and quantitative interpretation of fracture porosity," *Acta Geophysica Sinica*, vol. 39, no. 6, pp. 845–852, 1996.

[71] Y. Y. Yang, J. Lu, H. Y. Li, Q. M. Qi, and H. L. Zhou, "Fracture prediction based on walkaround 3D3C vertical seismic profiling data: a case study from the Tarim Basin in China," *Geophysics*, vol. 87, no. 4, pp. D123–D136, 2022.